Calcium Phosphate Deposition on Planar and Stepped (101) Surfaces of Anatase TiO$_2$: Introducing an Interatomic Potential for the TiO$_2$/Ca-PO$_4$/Water Interface

Giulia Mancardi,[†,‡] Carlos H. Tamargo,[‡] Umberto Terranova,[‡] and Nora H. De Leeuw[*,‡,†]

†Department of Chemistry, University College London, 20 Gordon Street, London WC1H 0AJ, UK

‡School of Chemistry, Cardiff University, Main Building, Park Place, Cardiff, CF10 3AT, UK

E-mail: deleeuwn@cardiff.ac.uk

Abstract

Titanium is commonly employed in orthopaedic and dental surgery, owing to its good mechanical properties. The titanium metal is usually passivated by a thin layer of its oxide and, in order to promote its integration with the biological tissue, it is covered by a bioactive material such as calcium phosphate (CaP). Here, we have investigated the deposition of calcium and phosphate species on the anatase phase of titanium dioxide (TiO_2) using interatomic potential-based molecular dynamics simulations. First, we have combined different force fields developed for CaP, TiO_2 and water, and benchmarked the results against density functional theory calculations. Based on our study, we consider that the new parameters can be used successfully to study the nucleation of CaP on realistic anatase and rutile TiO_2 nanoparticles, including surface defects.

Introduction

The first application of titanium in orthopaedic surgery dates back to the early fifties.[1] Nowadays, due to its high corrosion- and wear-resistance, lightness, the absence of allergic reactions and its mechanical reliability in aqueous environment, titanium and its alloys are commonly employed for load-bearing prostheses, such as hip joint and bone replacements, and artificial teeth.[2,3]

Unfortunately, titanium does not bond to the living tissue. For this reason, to promote its integration and minimize the risks related to the release of metallic ions into the body, titanium is usually coated by hydroxyapatite (HA), i.e. the calcium phosphate (CaP) which constitutes the main inorganic component of bone and tooth tissues. HA is commonly deposited as a 40-200 μm thick layer onto the metallic surface using the plasma spraying technique.[4] The coating can also be prepared through electrophoretic deposition,[5] sol-gel deposition,[6] electrochemical deposition,[7] sputtering,[8] hydrothermal synthesis[9] and biomimetic deposition.[10] The last technique consists of soaking the metallic implant in simulated body fluids (SBFs) at body temperature, to obtain a ceramic coating which is very similar to the

bone mineral.[11]

The high corrosion-resistance of the material stems from the passivation of titanium by a thin layer of its oxide. The most common polymorphs of TiO_2 are rutile and anatase.[12] Although rutile is the thermodynamically most stable bulk phase, at a nanometric scale the surface energy for anatase particles is lower than that of rutile particles of the same size,[13,14] and this increased stability of nanoparticulate anatase is the reason behind our choice of the anatase polymorph for this study.

Classical molecular dynamics (MD) simulations employing interatomic potentials (IP) can provide access to sizeable systems over time scales in the order of nanoseconds at a relatively low computational cost. Contrary to the much more expensive *ab initio* methods, the classical procedure relies on parameters calculated in advance, which reduce complex interatomic interactions to simple analytic equations. The derivation of these parameters is often the most significant effort in obtaining a classical description of the chemical processes.

In this work, we have consistently merged a force field for phosphate-based glasses[15] with the Matsui-Akaogi potential for anatase and rutile[16] as well as a set of parameters describing the interaction of their surfaces with water.[17] We found that this combination describes both the Ca^{2+} and PO_4^{3-} interactions with the most stable (101) surface of anatase to an acceptable degree compared to density functional theory calculations (DFT). Moreover, we have used the derived force field to obtain significant insight into the aggregation of Ca^{2+} and PO_4^{3-} ions on anatase. In summary, we propose the first classical description of the deposition processes occurring in a CaP-containing aqueous solution in contact with a TiO_2 surface.

Experimental Section

The results reported in this work have been performed using both DFT and IP methods with periodic boundary conditions.

Density functional theory calculations

The DFT code Vienna Ab initio Simulation Package (VASP), version 5.4.1,[18–21] was employed to derive the first-principles data needed to benchmark the proposed force field. We have used the generalized gradient approximation as derived by Perdew, Burke and Ernzerhof (PBE)[22] to account for the exchange-correlation energy. The PBE functional was combined with the Grimme correction to include the contribution of long-range dispersion interactions to the total energy of the system. We have used the latest modification of the Grimme's method, which incorporates geometry information into the *ab initio* parametrization of the dispersion coefficients and three-body terms to correct the overbinding of previous methods with only two-body contributions.[23–26] Energies were converged with Monkhorst-Pack k-points meshes of $8{\times}8{\times}4$ for the unit cell of anatase and $4{\times}4{\times}1$ for the slab representing the (101) surface of anatase.[27] Only the valence electrons were treated explicitly using a plane wave basis set with a cut-off energy of 400 eV. We have used the projected-augmented-wave method (PAW) to describe the nodal features of the valence electrons and their interaction with the inner core of the atom.[28,29] The convergence criterion for the electronic self-consistent iterations was set at 10^{-5} eV, whereas the threshold for the ionic forces was set at 0.03 eV/Å. To improve the electronic convergence, we have used the Gaussian smearing method with a band width of 0.1 eV.[30,31] The adsorption of calcium (or phosphate) on a TiO_2 slab results in a charged system. As there is a linear dependence between the total energy and the width of the vacuum layer that separates the periodic images of the slab owing to the interaction between the compensating background and the charged slab, we repeated the DFT optimizations with vacuum layers of 20 and 30 Å in order to check that the same minimum energy configuration was obtained regardless of the vacuum width. We also performed optimizations after removing a Ti^{4+} from the frozen core of the slab to counterbalance the positive charge from the two adsorbed Ca^{2+} ions, or, in the case of phosphate adsorption, we removed three O^{2-} ions from the frozen core of the slab to balance the -6 charge caused by the two adsorbed $PO_4{}^{3-}$ ions. The relative energy profiles are reported in

the ESI, Figures S6 for Ca^{2+} and S8 for $PO_4{}^{3-}$, from which it can be observed that the three sets of optimizations resulted in the same minimum energy configuration for both Ca^{2+} and $PO_4{}^{3-}$.

Interatomic potential simulations

To the best of our knowledge, a force field to study the deposition of CaP on a TiO_2 surface has not yet been reported. We overcame this limitation by combining a number of IP already in the literature. The CaP was modelled by the force field developed by Ainsworth *et al.*,[15] whilst the shell-model for water developed by De Leeuw and Parker[32] with the modification introduced by Kerisit and Parker[33] allowed us to introduce the aqueous medium.[34] For the description of the TiO_2, we selected the force field of Matsui and Akaogi,[16] which predicts the anatase phase to be more stable then rutile for sufficiently small nanoparticles.[35] It has been successfully employed by many authors[14,17,36–40] and gives unit cell parameters and the bulk modulus of anatase in excellent agreement with the experimental and DFT values (see ESI, Table S2). In both CaP and TiO_2 force fields, the atoms are subjected to short-range two-body interactions described by Buckingham potentials. We chose to use the same potential form for the missing cross terms, scaling the A parameter for the interactions between attractive (repulsive) atoms proportionally (inversely proportionally) to the ratio between the oxygen charges of TiO_2 and $PO_4{}^{3-}$, labelled respectively as O_{Ti} and O_{ph}:

$$A(\text{Ti}-\text{O}_{\text{ph}}) = A(\text{Ti}-\text{O}_{\text{Ti}}) \times \frac{q(\text{O}_{\text{ph}})}{q(\text{O}_{\text{Ti}})} \tag{1}$$

$$A(\text{O}_{\text{Ti}}-\text{O}_{\text{ph}}) = A(\text{O}_{\text{Ti}}-\text{O}_{\text{Ti}}) \times \frac{q(\text{O}_{\text{Ti}})}{q(\text{O}_{\text{ph}})} \tag{2}$$

$$A(\text{Ca}-\text{O}_{\text{Ti}}) = A(\text{Ca}-\text{O}_{\text{ph}}) \times \frac{q(\text{O}_{\text{Ti}})}{q(\text{O}_{\text{ph}})} \tag{3}$$

$$A(\text{P}-\text{O}_{\text{Ti}}) = A(\text{P}-\text{O}_{\text{ph}}) \times \frac{q(\text{O}_{\text{Ti}})}{q(\text{O}_{\text{ph}})} \tag{4}$$

where q is the charge of the atom type, $q(O_{ph})$ is taken from ref.[15] and $q(O_{Ti})$ from ref.[16]

The parameters for the water-TiO$_2$ interaction were taken from Alimohammadi *et al.*,[17] who derived the Lennard-Jones parameters for extended simple point charge[41] (SPC/E) water molecules interacting with TiO$_2$ surfaces described by the Matsui-Akaogi potentials.[16] The oxygen charge of water in the SPC/E and the shell-model differ only by 0.0476 e (electron charge) and for this reason, we did not scale the interactions between the oxygens of water and anatase. All the parameters used in this work are reported in the ESI, Table S1.

We ran the MD simulations using the DL_POLY package, version 4.07,[42] which easily allows the use of a customized force field. Each simulation consisted of an equilibration run of 25 ps in the NVE ensemble (constant number of particles, volume and energy) followed by 25 ps in the NVT ensemble (constant number of particles, volume and temperature), during which the Ca^{2+} and PO$_4{}^{3-}$ ions and the TiO$_2$ slab were kept frozen to allow the water to relax, and a subsequent 1 ns production run in the NPT ensemble (constant number of particles, pressure and temperature), when all species were free to move.[34] The radial distribution functions (RDFs) were collected between 0.75 and 1 ns. We chose a temperature of 310 K (body temperature) and a pressure of 1 bar. The timestep was set to 0.05 fs, which is compatible with the frequency of vibration of the core-shell units. We employed a cutoff of 8 Å and the Nosé-Hoover algorithm,[43,44] with a relaxation time of 0.1 ps for both the thermostat and the barostat. The amount of Ca^{2+} and PO$_4{}^{3-}$ ions was regulated to obtain a neutral system.

Planar and stepped (101) surfaces of anatase

The (101) plane is the most stable surface of anatase (Figure 1(a)). It presents two- and three-coordinated oxygen atoms (O$_{2c}$ and O$_{3c}$, respectively) and five- and six-coordinated titanium atoms (Ti$_{5c}$ and Ti$_{6c}$, respectively). The O$_{3c}$ and Ti$_{6c}$ sites have the same coordination environment of the bulk phase, whereas the O$_{2c}$ and Ti$_{5c}$ are unsaturated and therefore more reactive.
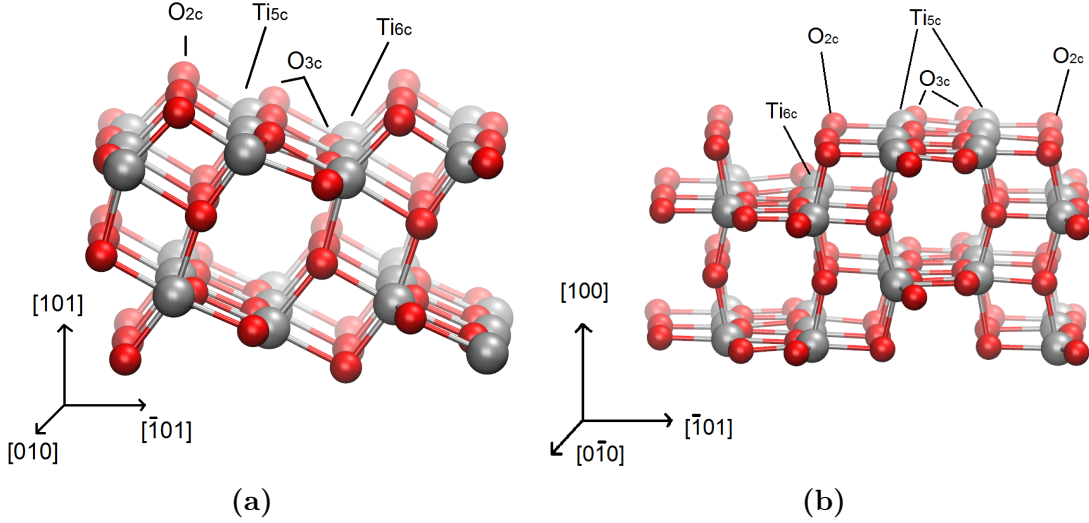
6

Figure 1: Anatase (a) (101) and (b) (100) surfaces. Titanium and oxygen atoms are labelled according to their coordination number. Color key: Ti:grey, O:red

The reactivity of metal oxides is influenced by the presence of defects at the surface.[12] Monoatomic step-edges on anatase (101) are common defects which have a characteristic trapezoidal shape.[45] The parallel sides of the trapezoidal islands are oriented along the [010] direction, whereas the other two sides along the [$\bar{1}$11] and [11$\bar{1}$]. The side of a step can itself be considered as a tiny slice of a surface, and follows its reactivity. Among all the possible step edges, we have considered the long parallel side of the trapezoidal islands, *i.e.* step B in ref.[46] (Figure S9, ESI), because its corresponding (100) surface has been extensively studied in the literature,[47,48] which is useful for comparison. Thus, we have also simulated the CaP deposition on the (100) surface of anatase (Figure 1(b)).

The (100) surface in Figure 1(b) exposes saturated Ti_{6c} and O_{3c} sites and undercoordinated Ti_{5c} and O_{2c} sites. Here, the Ti_{6c} are even less accessible than in the (101) surface because they are positioned in the recess of the saw-tooth orientation of the surface. When ordering the relaxed anatase surfaces in terms of their relative surface energies, the (100) surface follows after the (101). Surface energies are usually correlated to their reactivity and here depend on the density of exposed uncoordinated Ti atoms; thus we expect the (100) surface to be less stable but more reactive than the (101).[49]

Preparation of the TiO$_2$ slabs

The optimization of bulk anatase was performed employing both VASP and the IP-based General Utility Lattice Program (GULP) code, version 4.4.[50–52] The starting coordinates were taken from reference.[53]

Compared to experiment, the DFT and IP methods yielded values with errors of no more than 3% for the cell volume and vectors, bulk modulus and Ti−O bond distances and angles (see ESI, Table S2). We then used the DFT and IP optimized lattice parameters to construct the surface unit cells.

The anatase (101) and (100) surface slabs were created using the METADISE code, version 5.64,[54] which guarantees that no net dipole moment occurs normal to the surface.[55,56] For the DFT calculations, which were performed on the most stable (101) surface, the optimized (101) surface unit cell (Figure S1, ESI) was expanded 3 times along the [010] direction and 4 times along the [100] direction, resulting in a thickness of 12.9 Å (4 layers). We added a vacuum gap of 20 Å along [101] to avoid spurious interactions between the slab and its periodic images. The atoms in the two central layers of the slab were kept frozen at their bulk positions, whereas the top and the bottom layers were left free to rearrange. For the IP simulations, the GULP optimized structure was expanded 8 times along the [010] direction, 3 times along the [$\bar{1}$01] direction and 6 times along the [100] direction, resulting in a thickness of 17 Å (6 layers). The slab was centered in an orthorhombic box of approximately $30\times30\times77$ Å^3 and the space above and below the anatase slab was filled with a $30\times30\times30$ Å^3 cube of water. Similarly, the (100) surface unit cell obtained with METADISE was expanded 8 times along the [0$\bar{1}$0] direction, 3 times along [$\bar{1}$01] and 6 times along [100], resulting in a thickness of 21 Å (6 layers). The slab was centered in an orthorombic box with approximate dimension of $30 \times 29 \times 78$ Å^3.

A third slab was obtained rotating 14° clockwise the [$\bar{1}$01] axis of the (100) so that the new surface, labelled as (100)$_{rot}$, has mixed features between the (101) and the (100). Figure 2 shows all the slabs used for IP simulations and their relationship with the (101) surface.
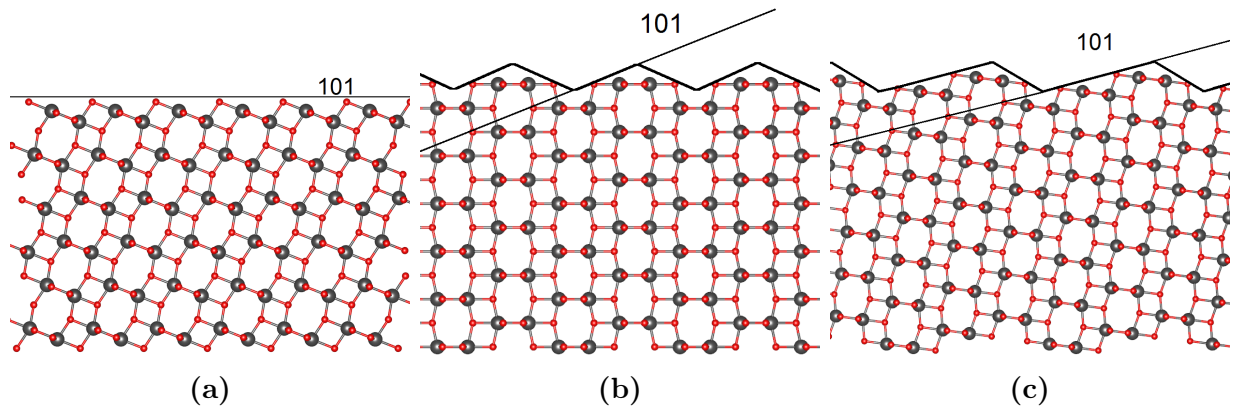
Figure 2: (a) (101), (b) (100) and (b) $(100)_{rot}$ surfaces and their relationship with the (101). Color key: Ti:grey, O:red

Results and Discussion

Water adsorption

Our first DFT calculations focused on the molecular adsorption of water, which has been previously shown to be favored over dissociative adsorption on the (101) surface of anatase.[57,58] In order to evaluate the sites for water adsorption on the surface, we placed a water molecule at the top and at the bottom of the slab on equivalent positions (see ESI, Figure S2 for the starting adsorption sites). After optimization, the water molecule preferentially adsorbed on three different sites (see Figure 3(a-c)).

In the most stable position, which matches that reported by previous studies in the literature,[59–62] the water molecule simultaneously interacts with a Ti_{5c} center via its O atom (hereafter referred as O_w) and with nearby O_{2c} sites through the formation of two hydrogen-bonds, as shown in Figure 3(a). The second most stable adsorption retains the $Ti_{5c}-O_w$ link but cleaves the hydrogen-bonds, leading to an energy penalty of 0.53 eV (Figure 3(b)). Finally, in the third position (Figure 3(c)), water binds the surface only via two hydrogen-bonds with the exposed O_{2c} sites, increasing the system energy by 1.34 eV compared to the most stable configuration. All the relative energies are reported in the ESI, Figure S3.

We next studied the change in the geometry of adsorbed water when the coverage is in-
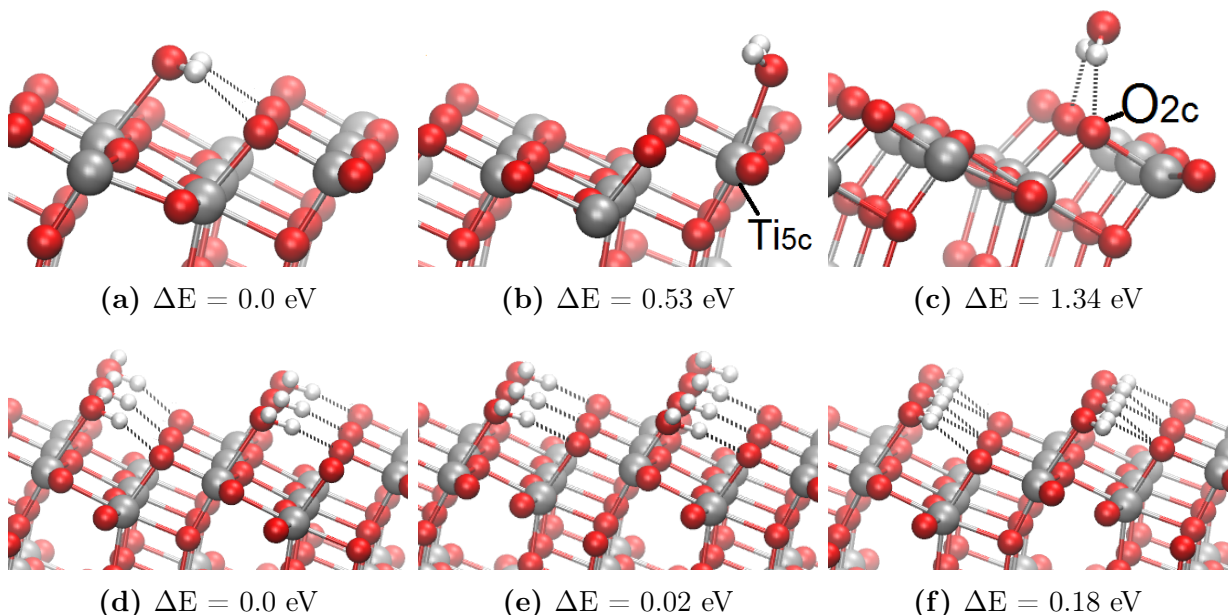
(a) $\Delta E = 0.0$ eV   **(b)** $\Delta E = 0.53$ eV   **(c)** $\Delta E = 1.34$ eV

(d) $\Delta E = 0.0$ eV   **(e)** $\Delta E = 0.02$ eV   **(f)** $\Delta E = 0.18$ eV

Figure 3: (a-c) DFT optimization of a single water adsorption on the anatase (101) surface. (d-f) DFT optimization of a monolayer of water on anatase (101). The energies of the adsorption configurations per water molecule are reported relative to the most stable system at each coverage. Color key: Ti:grey, O:red, H:white

Table 1: Interatomic distances between water and the anatase (101) surface. The DFT columns use the same letter labelling of Figure 3. The IP column reports the values obtained from the first peak of the RDFs obtained by classical MD.

Distances (Å)	DFT						IP
	(a)	(b)	(c)	(d)	(e)	(f)	
$Ti_{5c}-O_w$	2.28	2.26	/	2.31	2.32	2.31	2.15
$O_{2c}-H_w$	2.23	/	1.99	2.04-2.07	2.04	2.12	2.25

creased to a full monolayer. We tested several orientations for the water molecules using the structural information from the single molecule adsorption (see Figure S4, ESI), obtaining the full-coverage configurations reported in Figure 3(d), 3(e) and 3(f). In the lowest energy geometry, all water molecules adsorbed on Ti_{5c} sites are slightly rotated and form a single short hydrogen bond with the O_{2c} atoms, while the water molecules' dipole moments are oriented in a zig-zag fashion along the $[\bar{1}01]$ direction (Figure 3(d)). The alternative configuration with all dipole moments oriented in the same direction is only 0.02 eV higher in energy (see Figure 3(e)). In the least stable configuration, the number of hydrogen bonds is

maximized at the expense of their lengths. From the DFT distances reported in Table 1, it is possible to see that, in general, the adsorption of a monolayer of water on Ti_{5c} sites results in the elongation of the $Ti_{5c}-O_w$ bond and a shortening of the hydrogen bond $O_{2c}-H_w$. Similar to the single molecule adsorption, the full coverage results agree qualitatively with those in the literature.[60,61,63]

The input for the MD simulations was prepared as described in the section named "Preparation of the TiO_2 slabs". The resulting RDFs are reported in Figures S10-11, ESI.

Table 2: Interatomic distances between water and the (100) and $(100)_{rot}$ surfaces of anatase. The DFT distances[46] for molecular adsorption of water on the anatase (100) surface are also reported.

Distances (Å)	IP		DFT[46]
	(100)	$(100)_{rot}$	
$Ti_{5c}-O_w$	2.15	2.15	2.282
$O_{2c}-H_w$	2.25	2.25	2.141

We obtained average $Ti_{5c}-O_w$ and $O_{2c}-H_w$ distances of 2.15 and 2.25 Å, respectively, which is in acceptable agreement with the DFT results (Tables 1 and 2). Figure 4 shows a snapshot after 1 ns of NPT simulation. The first monolayer of adsorbed water interacts with the anatase surface in configurations that resemble the DFT orientations in Figures 3(d) and 3(e). As expected, these water molecules do not only establish hydrogen-bonds with the O_{2c} sites, but also with other water molecules from the aqueous medium. However, this first monolayer of water remains bound to the surface and no exchange with the water molecules from the second layer is observed. This is in agreement with the experimental findings that when 0.20 and 0.92 monolayers are annealed from 80 K to 190 K, the 0.20 arrangement looses its clustered structure while the 0.92 monolayer does not show appreciable changes.[64] In addition to the water that binds directly to the Ti_{5c} centers, other water molecules adsorb more loosely via hydrogen-bonds with the O_{2c} sites, forming semi-ordered rows along the [010] direction. A similar arrangement of water has been found previously by DFT methods for a 2 monolayer coverage.[60] In addition, this second layer of water that is less strongly bound to the surface may explain the mobile precursor responsible for transient diffusion of

water at 80 K.[64] These results highlight the good transferability of the force field to describe the water-anatase interface using water models different from the original SPC/E.
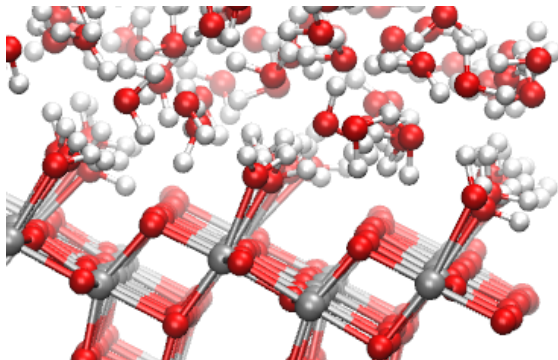

Figure 4: Classical MD snapshot after 1 ns in an NPT ensemble showing water adsorption on the anatase (101) surface. Color key: Ti:grey, O:red, H:white

Calcium phosphate adsorption

We started by adsorbing two Ca^{2+} ions, one at the top and one at the bottom of the anatase slab at equivalent positions. The optimizations led to only two low-energy adsorption sites for the Ca^{2+} ion: one where it can coordinate two O_{2c} and one O_{3c} (Figure 5(a)), and another on top of a Ti_{6c} coordinating two O_{2c} (Figure 5(b)). The first position is 1.23 eV more stable than the second. We verified that the energetic stability of the different adsorption sites does not depend either on the vacuum size or the charge of the system by performing single point calculations increasing the vacuum from 20 to 30 Å and using a neutral slab (see ESI, Figures S5-S6). We report in Table 3 the distances between the Ca^{2+} ion and the atoms of the surface.

During the MD simulations the Ca^{2+} ions are in a position very similar to that of the lowest energy structure obtained by DFT. In particular, they adsorb exactly on top of two consecutive O_{2c} and their partial solvation results in longer $O_{2c}-Ca$ bonds than in the anhydrous DFT optimization, whereas in addition, Ca^{2+} ions are able to displace the water that is loosely interacting with the O_{2c} sites through hydrogen-bonds (see Figure 6 and Table 3).
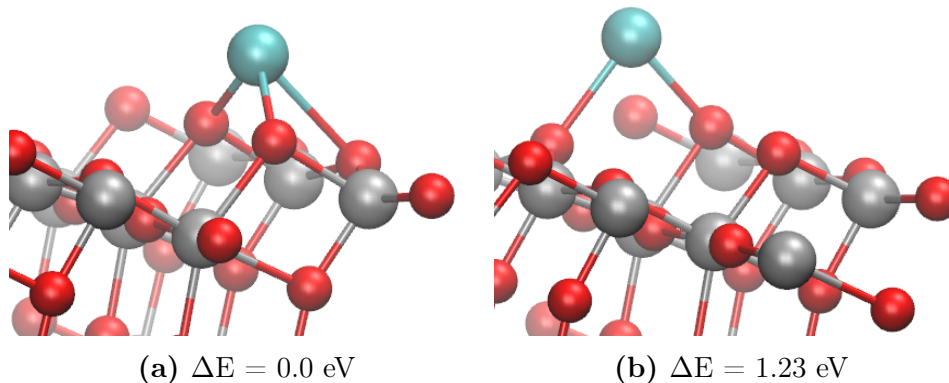
(a) $\Delta E = 0.0$ eV   **(b)** $\Delta E = 1.23$ eV

Figure 5: DFT optimization of Ca^{2+} adsorption on the anatase (101) surface. The adsorption energies of the configurations are reported relative to the most stable position. Color key: Ti:grey, O:red, Ca:cyan.
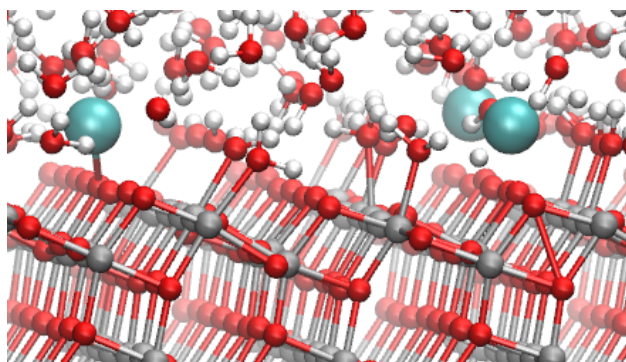

Figure 6: Classical MD simulation of Ca^{2+} adsorption on the anatase (101) surface. Color key: Ti:grey, O:red, H:white, Ca:cyan.

For $PO_4{}^{3-}$, seven different starting configurations were considered (see ESI, Figure S7), which reduced to four after DFT geometry optimization. The corresponding structures and their relative energies are reported in Figure S8 of ESI, which shows that, as in the case of the Ca^{2+} ion, the vacuum size and the charge of the system do not influence the trend in energy differences among the structures. The two lowest energy configurations and the relative $Ti_{5c}-O_{ph}$ distances are reported in Figure 7 and Table 4.

During the MD simulations, we found that the $PO_4{}^{3-}$ ions adsorb on the anatase surface only in the presence of Ca^{2+} ions. This behavior reflects the experimental CaP nucleation on TiO_2, where the initial adsorption of Ca^{2+} ions on the oxide is followed by the deposition of $PO_4{}^{3-}$ ions onto the positively charged layer.[65,66] When a $PO_4{}^{3-}$ ion adsorbs on the surface,

Table 3: Interatomic distances between calcium and the anatase (101) surface. The DFT columns use the same letter labelling of Figure 5.

Distances (Å)	DFT		IP
	(a)	(b)	
O_{2c}−Ca	2.21	2.12	2.25
O_{2c}−Ca	/	2.29	/
O_{3c}−Ca	2.54	/	3.35

its geometry agrees with that predicted by DFT (compare Figures 7(a) and 8(a)), *i.e.* two O_{ph} bridge two consecutive Ti_{5c} along the [010] direction. The Ti_{5c}−O_{ph} distance obtained from the RDF is only 0.03 Å shorter than the one obtained by DFT optimization (see Table 4). Another possibility for the $PO_4{}^{3-}$ ion is to coordinate a Ca^{2+} ion already adsorbed on the oxide surface (see Figure 8(b)). The average Ca−O_{ph} distance for the structures in Figures 8(a) and 8(b) are respectively 2.25 and 2.35 Å. These distances are shorter than 2.45 Å, which is the value obtained using classical[15,34] and *ab initio* MD[67] to simulate CaP species in solution. The shortening is likely to be due to the geometric restraint imposed by the proximity of the surface active sites.
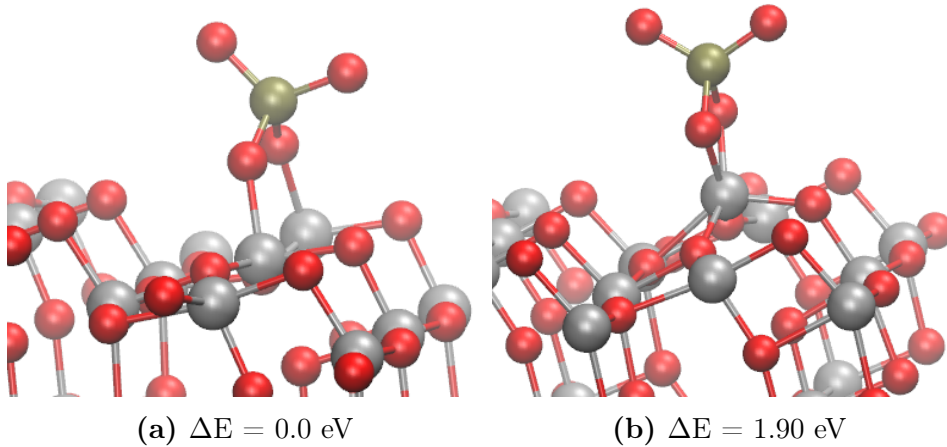

(a) $\Delta E = 0.0$ eV   **(b)** $\Delta E = 1.90$ eV

Figure 7: DFT optimized structures of $PO_4{}^{3-}$ adsorption on the anatase (101) surface. The energy of the configurations are reported relative to the most stable position. Color key: Ti:grey, O:red, P:green.
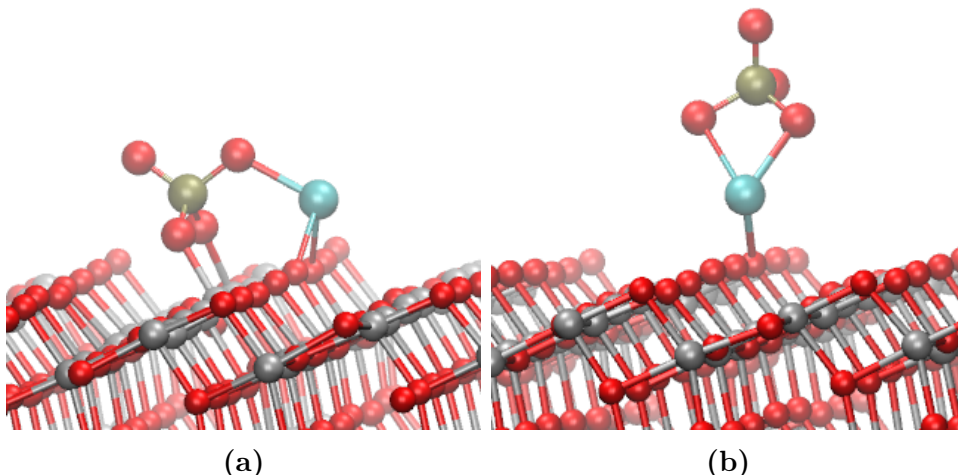
Figure 8: Classical MD simulation snapshots of Ca^{2+} and PO_4^{3-} adsorption on the anatase (101) surface. Water molecules are removed for clarity. Color key: Ti:grey, O:red, P:green.

Table 4: Interatomic distances between PO_4^{3-} and the anatase (101) surface. The DFT columns use the same letter labelling of Figure 7.

Distance (Å)	DFT		IP
	(a)	(b)	
$Ti_{5c}-O_{ph}$	1.88	1.94	1.85

Calcium phosphate deposition on planar and stepped surfaces

Finally, we have employed the validated force field introduced in section "Interatomic Potential simulations" and reported in Table S1 of the ESI to model the deposition of Ca^{2+} and PO_4^{3-} ions in aqueous solution on the anatase (101), (100) and $(100)_{rot}$ surfaces. We consider the present set of interatomic potentials as a first proposition to describe the adsorption of CaP on anatase (101). Therefore, although water tends to dissociate on the (100) surface, we have decided to initially overlook the dissociation of water, focusing instead on the molecular adsorption only. This scheme also allows to observe the adsorption of CaP on the TiO_2 surfaces, because there are no terminal OH groups hindering the direct TiO_2-CaP interaction. Note that due to the use of a classical force field, the terminal OH groups cannot re-form water and desorb from the surface in order to leave vacant Ti_{5c} and O_{2c} sites for the incoming CaP ions. We expect to expand this set of interatomic potential in a second report, where an additional atom type for oxygen will be included to describe the OH groups

dissociated on the TiO$_2$ surface.

We placed 9 Ca^{2+} ions above and 9 Ca^{2+} ions below the slab, at $\sim$ 2 Å from the surfaces. The space between the slabs was filled with water and the necessary number of PO$_4$$^{3-}$ ions to neutralize the positive charge given by the Ca^{2+} ions. Figure 9 shows snapshots of the three different surfaces taken after 1 ns. The RDFs and the average coordination numbers are plotted in Figures S15-16, ESI and listed in Table 5. Our simulations show that aggregation and deposition take place concurrently on the (101) surface (Figure 9(a)), whereas the Ca^{2+} and PO$_4$$^{3-}$ ions prefer to bind to the (100) surface rather than aggregate in solution (Figure 9(b)). The anatase (100) facet is known to be more reactive than the (101) towards the adsorption of water, methanol and formic acid.[59] This tendency is confirmed by an increase in the coordination number for the Ca$-$O$_{Ti}$, Ca$-$Ti, O$_{ph}$$-O_{Ti}$ and O$_{ph}$$-$Ti pairings on the (100) surface with respect to the (101). The Ca$-$O$_{ph}$ pairing, which measures CaP aggregation, exhibits the opposite trend (see Table 5).
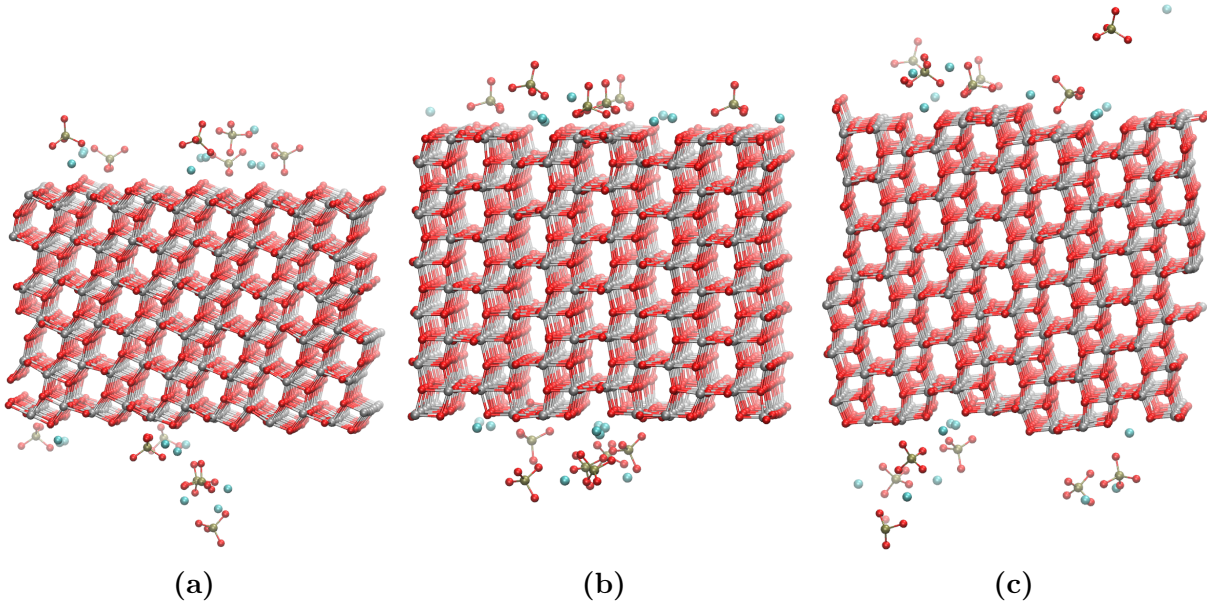

(a)   **(b)**   **(c)**

Figure 9: Classical MD snapshots of CaP deposition on (a) anatase (101), (b) (100) and (c) (100)$_{rot}$ surface. Water molecules are removed for clarity. Color key: Ti:grey, O:red, Ca:cyan, P:green.

Table 5: Interatomic distances for the adsorption of Ca^{2+} and PO_4^{3-} ions on the anatase (101), (100) and (100)$_{rot}$ surfaces.

Distance (Å)	(101)	(100)	(100)$_{rot}$
$Ca-O_{2c}$	2.25	2.35	2.35
$Ca-Ti_{5c}$	3.45	3.75	3.75
$Ca-O_{ph}$	2.35	2.25	2.35
$O_{ph}-O_{2c}$	2.65	2.65	2.75
$O_{ph}-Ti_{5c}$	1.85	1.95	1.95

On the (100) surface, Ca^{2+} ions tend to coordinate to the exposed O_{2c} sites at the edge of the gulleys (see Figure 10). The PO_4^{3-} adsorb preferentially on the relatively flat regions of the (100) surface, which present two parallel rows of unsaturated positive Ti_{5c} ions that are capable of coordinating the three O_{ph} atoms simultaneously (Figure 10). The (101) and (100) surfaces have similar features, which can be described by an outer layer that is formed of rows of Ti_{5c} atoms along the [010] direction that bind O_{2c} and O_{3c} sites, and rows of O_{2c} atoms along the same direction that bridge Ti_{5c} and Ti_{6c} sites (see Figure 4). Therefore, although the (101) and (100) surfaces differ in the number of alternating rows of nucleophilic (O_{2c}) and electrophilic (Ti_{5c}) sites along the [$\bar{1}$01] direction, both surfaces should show a similar behavior towards the adsorption of CaP, and hence we can expect that the parameters used to describe the $CaP-TiO_2$ interaction on (101) will also work for (100). Previous works have shown that parameters initially refined for the (101) surface of anatase have satisfactorily performed for other surfaces, not just of anatase but also rutile.[17] As shown in Figure 2, the (100)$_{rot}$ surface has mixed features of both the (101) and (100) surfaces, and indeed it exhibits intermediate behavior towards CaP deposition (Figure 9(c)).
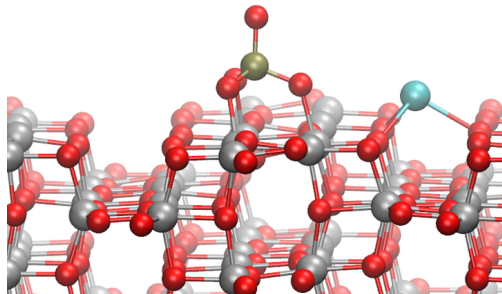
Figure 10: Classical MD snapshot of CaP deposition on anatase (100). The preferred adsorption sites for the Ca^{2+} and PO_4^{3-} ions are visible. Color key: Ti:grey, O:red, Ca:cyan, P:green.

Moving from anatase (101) to the (100) surface, we observe that the coordination numbers $Ca-O_{2c}$ and $O_{ph}-Ti_{5c}$ increase by 130% and 72%, respectively, causing a stretching of 0.1 Å in the distances $Ca-O_{2c}$ and $O_{ph}-Ti_{5c}$ (see Table 5). Furthermore, during the deposition of CaP, the displacement of water was more pronounced on (100) than on (101), as reported in Table 6, in Figures S12-14 and S17 (ESI). In fact, upon adsorption of the ions, the $Ti-O_w$ coordination number decreases by $\approx$ 12% on (101) and 20% on (100). These modifications indicate that anatase (100) is more reactive than (101) towards the adsorption of CaP. We explain the higher reactivity of (100) over (101) after considering the effect of the distribution of active sites on both surfaces, namely Ti_{5c} and O_{2c}, on the adsorption strength of water and CaP ions.

The (101) and (100) surfaces differ in their arrangements of the active sites, *i.e.* the species O_{2c} and Ti_{5c} which are undercoordinated with respect to the bulk. The (101) surface presents an alternation of positive and negative sites along the $[\bar{1}01]$ direction ($\cdots O_{2c}$-Ti_{5c}-O_{2c}-$Ti_{5c}\cdots$) with the O_{2c} sites at the tip of the sawtooth-like corrugations (see Figure 1(a)). This arrangement allows water to interact simultaneously with the Ti_{5c} sites, via direct $Ti_{5c}-O_w$ links, and with the O_{2c} sites through hydrogen-bonds, as shown in Figure 3(d) and Figure 4. In contrast, the (100) surface shows a distribution that places the Ti_{5c} and O_{2c} sites on the same plane ($\cdots$gulley-O_{2c}-Ti_{5c}-Ti_{5c}-O_{2c}-gulley$\cdots$), see Figure 1(b), thus reducing the possibility for the water molecules to interact simultaneously with both centers. Consequently, the water molecules have a stronger adsorption on (101) than on (100),

and hence they are harder to displace by the incoming CaP ions. Note that, although the discussed $O_w-H\cdots O_{2c}$ hydrogen-bonds on (101) are partially disrupted by the presence of bulk water, they are still observable during the MD simulations. This finding is in agreement with the DFT calculations by Gong and Selloni, who have shown that adsorption is energetically favored on (101) over (100) by 0.18 eV (by 0.13 eV if the dissociative adsorption of water on (100) is considered).[59] Water molecules adsorb molecularly on (101), but can dissociate on (100). The dissociative adsorption on (100) should cause a greater hindrance to the displacement of water by the deposition of CaP, because the water molecules have to assemble again before desorbing from the surface, which requires additional energy.

The arrangement of active sites on (101) and (100) has an opposite effect on the adsorption of CaP ions compared to water. On the (101) surface, the Ca^{2+} ion can only bind two O_{2c} sites simultaneously, placing itself on top of the sawtooth-like corrugations (see Figure 5(a)). In comparison, on the (100) surface, the Ca^{2+} ions can bind three O_{2c} sites at the gulleys; the short spacing between the O_{2c} centres, and their zig-zag distribution along the $[0\bar{1}0]$ direction allows this favourable adsorption. Furthermore, whereas on (101) Ca^{2+} needs to compete with the water that is interacting simultaneously with the Ti_{5c} and O_{2c} centres plus the more loosely adsorbed water that only interacts via hydrogen-bonds with O_{2c} sites, on (100) Ca^{2+} only needs to displace the weakly hydrogen-bounded water at the gulleys. Regarding the PO_4 ions, a similar reasoning can be applied. On (101), the PO_4 ion, which has four negative centers at each corner of the tetrahedron available for interaction with the Ti_{5c} sites, can adsorb on no more than two Ti_{5c} centers (Figure 7(a) and Figure 8(a)). On (100), the flat regions between gulleys provide a more favourable Ti_{5c} zig-zag arrangement, with Ti_{5c}-Ti_{5c} spacings shorter than 4 Å, where the PO_4 can adsorb via three O_{ph}-Ti_{5c} links (Figure 10). Therefore, the stronger CaP interaction with the (100) surface produces a higher amount of displaced water compared to (101). Again, it is important to note that these conclusions are derived from MD simulations, where only molecular adsorption was considered.

Based on the results above, we expect a corresponding increase in CaP deposition at the steps B compared to the clean substrate. When considering the slightly rotated $(100)_{rot}$ surface, which has features of both the (100) and the (101) surfaces, the reactivity towards CaP deposition lies about halfway between the (100) and the (101) facets, suggesting that the plain (100) surface may actually exhibit higher reactivity than step B.

Table 6: Difference in coordination number of $Ti_{5c}-O_w$ with and without calcium and phosphate ions.

	[101]	[100]	$[100]_{rot}$
CN $Ti_{5c}-O_w$	1.000	1.000	1.000
CN $Ti_{5c}-O_w$ with ions	0.884	0.804	0.916
Difference	-0.116	-0.196	-0.084

Summary and Conclusions

In the present work, we have combined existing force fields for CaP, TiO_2 and water, and added missing two-body interactions between CaP and TiO_2, to perform classical MD simulations of CaP deposition on anatase in aqueous solution. The comparison with DFT shows very good performance of the new set of parameters in describing the adsorption of CaP on the most stable (101) surface of anatase. The (100) surface of anatase, which has the same features of one of the steps present in the trapezoidal islands observed experimentally on the (101) surface, was shown to be more reactive than the (101) towards CaP deposition. This finding was explained considering the different distribution of active sites on the two surfaces, which affects both water adsorption as well as calcium and phosphate deposition in opposing ways.

Associated content

Supporting Information Parameters for the combined force field for calcium phosphate solution in water in contact with an anatase surface; DFT optimization: H_2O adsorption,

Ca^{2+} adsorption, PO$_4$$^{3-}$ adsorption; Step edges on the anatase (101) surface; Water adsorption on anatase surfaces; Water adsorption on anatase surfaces in presence of calcium and phosphate ions; Calcium phosphate deposition on Anatase (101), (100) and (100)$_{rot}$ surfaces; Comparison of Radial Distribution Functions collected between 0 - 0.25 ns and 0.75 - 1 ns; Electrostatic Energy, Cell volume and Temperature variation during calcium phosphate deposition on anatase (101), anatase (100) and anatase (100)$_{rot}$ surfaces.

Acknowledgement

References

(1) Laing, P. In *Corrosion and Degradation of Implant Materials*; Syrett, B. C., Acharya, A., Eds.; American Society for Testing and Materials, 1979; Vol. 684; pp 199–211.

(2) Chandra, A.; Ryu, J. J.; Karra, P.; Shrotriya, P.; Tvergaard, V.; Gaisser, M.; Weik, T. Life expectancy of modular Ti6Al4V hip implants: Influence of stress and environment. *J. Mech. Behav. Biomed. Mater.* **2011**, *4*, 1990–2001.

(3) Suchanek, W.; Yoshimura, M. Processing and properties of hydroxyapatite-based biomaterials for use as hard tissue replacement implants. *J. Mater. Res.* **1998**, *13*, 94–117.

(4) de Groot, K.; Wolke, J. G.; Jansen, J. A. Calcium phosphate coatings for medical implants. *Proc. Inst. Mech. Eng. H* **1998**, *212*, 137–147.

(5) Ducheyne, P.; Van Raemdonck, W.; Heughebaert, J. C.; Heughebaert, M. Structural analysis of hydroxyapatite coatings on titanium. *Biomaterials* **1986**, *7*, 97–103.

(6) Kim, H. W.; Koh, Y. H.; Li, L. H.; Lee, S.; Kim, H. E. Hydroxyapatite coating on titanium substrate with titania buffer layer processed by sol-gel method. *Biomaterials* **2004**, *25*, 2533–2538.

(7) Shirkhanzadeh, M. Electrochemical fabrication of bioactive composite coatings on Ti6A14V surgical alloy. *Mater. Lett.* **1992**, *14*, 27–30.

(8) Ong, J. L.; Lucas, L. C.; Lacefield, W. R.; Rigney, E. D. Structure, solubility and bond strength of thin calcium phosphate coatings produced by ion beam sputter deposition. *Biomaterials* **1992**, *13*, 249–254.

(9) Lorenzetti, M.; Dakischew, O.; Trinkaus, K.; Lips, K. S.; Schnettler, R.; Kobe, S.; Novak, S. Enhanced osteogenesis on titanium implants by UVB photofunctionalization of hydrothermally grown TiO2 coatings. *J. Biomater. Appl.* **2015**, *30*, 71–84.

(10) Hata, K.; Kokubo, T.; Nakamura, T.; Yamamuro, T. Growth of a Bonelike Apatite Layer on a Substrate by a Biomimetic Process. *J. Am. Ceram. Soc.* **1995**, *78*, 1049–1053.

(11) Barrère, F.; Layrolle, P.; Van Blitterswijk, C. A.; De Groot, K. Biomimetic calcium phosphate coatings on Ti6Al4V: A crystal growth study of octacalcium phosphate and inhibition by Mg2+ and HCO3 -. *Bone* **1999**, *25*, 107S–111S.

(12) Diebold, U. The surface science of titanium dioxide. *Surf. Sci. Rep.* **2003**, *48*, 53–229.

(13) Zhang, H. Z.; Banfield, J. F. Thermodynamic analysis of phase stability of nanocrystalline titania. *J. Mater. Chem.* **1998**, *8*, 2073–2076.

(14) Naicker, P. K.; Cummings, P. T.; Zhang, H.; Banfield, J. F. Characterization of Titanium Dioxide Nanoparticles Using Molecular Dynamics Simulations. *J. Phys. Chem. B* **2005**, *109*, 15243–15249.

(15) Ainsworth, R. I.; Di Tommaso, D.; Christie, J. K.; de Leeuw, N. H. Polarizable force field development and molecular dynamics study of phosphate-based glasses. *J. Chem. Phys.* **2012**, *137*, 234502.

(16) Matsui, M.; Akaogi, M. Molecular Dynamics Simulation of the Structural and Physical Properties of the Four Polymorphs of TiO2. *Mol. Simul.* **1991**, *6*, 239–244.

(17) Alimohammadi, M.; Fichthorn, K. A. A Force Field for the Interaction of Water with TiO2 Surfaces. *J. Phys. Chem. C* **2011**, *115*, 24206–24214.

(18) Kresse, G.; Hafner, J. Ab initio molecular dynamics for liquid metals. *Phys. Rev. B* **1993**, *47*, 558–561.

(19) Kresse, G.; Hafner, J. Ab initio molecular-dynamics simulation of the liquid-metal-amorphous-semiconductor transition in germanium. *Phys. Rev. B* **1994**, *49*, 14251–14269.

(20) Kresse, G.; Furthmüller, J. Efficiency of ab-initio total energy calculations for metals and semiconductors using a plane-wave basis set. *Comput. Mater. Sci.* **1996**, *6*, 15–50.

(21) Kresse, G.; Furthmüller, J. Efficient iterative schemes for ab initio total-energy calculations using a plane-wave basis set. *Phys. Rev. B* **1996**, *54*, 11169–11186.

(22) Perdew, J. P.; Burke, K.; Ernzerhof, M. Generalized Gradient Approximation Made Simple. *Phys. Rev. Lett.* **1996**, *77*, 3865–3868.

(23) Grimme, S. Semiempirical GGA-Type Density Functional Constructed with a Long-Range Dispersion Correction. *J. Comput. Chem.* **2006**, *27*, 1787–1799.

(24) Grimme, S.; Antony, J.; Ehrlich, S.; Krieg, H. A consistent and accurate ab initio parametrization of density functional dispersion correction (DFT-D) for the 94 elements H-Pu. *J. Chem. Phys.* **2010**, *132*, 154104.

(25) Ambrosetti, A.; Alfè, D.; Distasio, R. A.; Tkatchenko, A. Hard numbers for large molecules: Toward exact energetics for supramolecular systems. *J. Phys. Chem. Lett.* **2014**, *5*, 849–855.

(26) Grimme, S.; Ehrlich, S.; Goerigk, L. Effect of the Damping Function in Dispersion Corrected Density Functional Theory. *J. Comput. Chem.* **2011**, *32*, 1456–1465.

(27) Monkhorst, H. J.; Pack, J. D. Special points for Brillouin-zone integrations. *Phys. Rev. B* **1976**, *13*, 5188–5192.

(28) Blochl, P. Projector augmented-wave method. *Phys. Rev. B* **1994**, *50*, 17953–17979.

(29) Kresse, G. From ultrasoft pseudopotentials to the projector augmented-wave method. *Phys. Rev. B* **1999**, *59*, 1758–1775.

(30) Ho, K.; Fu, C.; Harmon, B.; Weber, W.; Hamann, D. Vibrational Frequencies and Structural Properties of Transition Metals via Total-Energy Calculations. *Phys. Rev. Lett.* **1982**, *49*, 673–676.

(31) Fu, C. L.; Ho, K. M. First-principles calculation of the equilibrium ground-state properties of transition metals: Applications to Nb and Mo. *Phys. Rev. B* **1983**, *28*, 5480–5486.

(32) de Leeuw, N. H.; Parker, S. C. Molecular-dynamics simulation of MgO surfaces in liquid water using a shell-model potential for water. *Phys. Rev. B* **1998**, *58*, 13901–13908.

(33) Kerisit, S.; Parker, S. C. Free energy of adsorption of water and calcium on the {1014} calcite surface. *J. Am. Chem. Soc.* **2004**, *126*, 10152–10161.

(34) Mancardi, G.; Hernandez Tamargo, C. E.; Di Tommaso, D.; de Leeuw, N. H. Detection of Posner's clusters during calcium phosphate nucleation: a molecular dynamics study. *J. Mater. Chem. B* **2017**, *5*, 7274–7284.

(35) Zhou, Y.; Fichthorn, K. A. Microscopic view of nucleation in the anatase-to-rutile transformation. *J. Phys. Chem. C* **2012**, *116*, 8314–8321.

(36) Oliver, P.; Watson, G.; Kelsey, E.; Parker, S. Atomistic simulation of the surface structure of the TiO2 polymorphs rutile and anatase. *J. Mater. Chem.* **1997**, *7*, 563–568.

(37) Swamy, V.; Gale, J.; Dubrovinsky, L. Atomistic simulation of the crystal structures and bulk moduli of TiO2 polymorphs. *J. Phys. Chem. Solids* **2001**, *62*, 887–895.

(38) Predota, M.; Bandura, A. V.; Cummings, P. T.; Kubicki, J. D.; Wesolowski, D. J.; Chialvo, A. A.; Machesky, M. L. Electric Double Layer at the Rutile (110) Surface. 1. Structure of Surfaces and Interfacial Water from Molecular Dynamics by Use of ab Initio Potentials. *J. Phys. Chem. B* **2004**, 12049–12060.

(39) Koparde, V. N.; Cummings, P. T. Molecular dynamics simulation of titanium dioxide nanoparticle sintering. *J. Phys. Chem. B* **2005**, *109*, 24280–24287.

(40) Alimohammadi, M.; Fichthorn, K. A. Molecular dynamics simulation of the aggregation of titanium dioxide nanocrystals: Preferential alignment. *Nano Lett.* **2009**, *9*, 4198–4203.

(41) Berendsen, H. J. C.; Grigera, J. R.; Straatsma, T. P. The Missing Term in Effective Pair Potentials. *J. Phys. Chem.* **1987**, *91*, 6269–6271.

(42) Todorov, I. T.; Smith, W.; Trachenko, K.; Dove, M. T. DL_POLY_3: new dimensions in molecular dynamics simulations via massive parallelism. *J. Mater. Chem.* **2006**, *16*, 1911–1918.

(43) Nosé, S. A unified formulation of the constant temperature molecular dynamics methods. *J. Chem. Phys.* **1984**, *81*, 511–519.

(44) Hoover, W. G. Canonical dynamics: Equilibrium phase-space distributions. *Phys. Rev. A* **1985**, *31*, 1695–1697.

(45) Hebenstreit, W.; Ruzycki, N.; Herman, G. S.; Gao, Y.; Diebold, U. Scanning tunneling microscopy investigation of the TiO2 anatase (101) surface. *Phys. Rev. B* **2000**, *62*, R16334–R16336.

(46) Gong, X.-Q.; Selloni, A.; Batzill, M.; Diebold, U. Steps on anatase TiO2(101). *Nat. Mater.* **2006**, *5*, 665–670.

(47) Mendive, C. B.; Bredow, T.; Feldhoff, A.; Blesa, M. A.; Bahnemann, D. Adsorption of oxalate on anatase (100) and rutile (110) surfaces in aqueous systems: experimental results vs. theoretical predictions. *Phys. Chem. Chem. Phys.* **2009**, *11*, 1794.

(48) Jensen, S.; Kilin, D. Anatase (100) thin film surface computational model for photoelectrochemical cell. *Int. J. Quantum Chem.* **2012**, *112*, 3874–3878.

(49) Lazzeri, M.; Vittadini, A.; Selloni, A. Structure and energetics of stoichiometric TiO2 anatase surfaces. *Phys. Rev. B* **2001**, *63*, 155409.

(50) Gale, J. D. GULP: A computer program for the symmetry-adapted simulation of solids. *J.Chem. Soc., Faraday Trans.* **1997**, *93*, 629–637.

(51) Gale, J. D.; Rohl, A. L. The General Utility Lattice Program (GULP). *Mol. Simul.* **2003**, *29*, 291–341.

(52) Gale, J. D. GULP: Capabilities and prospects. *Zeitschrift fur Kristallographie* **2005**, *220*, 552–554.

(53) Rezaee, M.; Mousavi Khoie, S. M.; Liu, K. H. The role of brookite in mechanical activation of anatase-to-rutile transformation of nanocrystalline TiO2: An XRD and Raman spectroscopy investigation. *CrystEngComm* **2011**, *13*, 5055–5061.

(54) Watson, G. W.; Kelsey, E. T.; de Leeuw, N. H.; Harris, D. J.; Parker, S. C. Atomistic simulation of dislocations, surfaces and interfaces in MgO. *J. Chem. Soc., Faraday Trans.* **1996**, *92*, 433–438.

(55) Buckingham, R. The classical equation of state of gaseous helium, neon and argon. *Proc. Royal Soc. Lond.* **1938**, *168*, 264–283.

(56) Sanders, M. J.; Leslie, M.; Catlow, C. R. A. Interatomic potentials for SiO2. *J. Chem. Soc., Chem. Commun.* **1984**, *4*, 1271–1273.

(57) Vittadini, A.; Selloni, A.; Rotzinger, F. P.; Grätzel, M. Structure and Energetics of Water Adsorbed at TiO2 Anatase (101) and (001) Surfaces. *Phys. Rev. Lett.* **1998**, *81*, 2954–2957.

(58) Barnard, A. S.; Zapol, P.; Curtiss, L. A. Modeling the Morphology and Phase Stability of TiO2 Nanocrystals in Water. *J. Chem. Theory Comput.* **2005**, *1*, 107–116.

(59) Gong, X. Q.; Selloni, A. Role of steps in the reactivity of the anatase TiO2(101) surface. *J. Catal.* **2007**, *249*, 134–139.

(60) Terranova, U.; Bowler, D. R. Effect of hydration of the TiO2 anatase (101) substrate on the atomic layer deposition of alumina films. *J. Mater. Chem* **2011**, *21*, 4197–4203.

(61) Arrouvel, C.; Digne, M.; Breysse, M.; Toulhoat, H.; Raybaud, P. Effects of morphology on surface hydroxyl concentration: A DFT comparison of anatase-TiO2 and γ -alumina catalytic supports. *J. Catal.* **2004**, *222*, 152–166.

(62) Gala, F.; Agosta, L.; Zollo, G. Water Kinetics and Clustering on the (101) TiO2 Anatase Surface. *J. Phys. Chem. C* **2016**, *120*, 450–456.

(63) Tilocca, A.; Selloni, A. Vertical and lateral order in adsorbed water layers on anatase TiO 2(101). *Langmuir* **2004**, *20*, 8379–8384.

(64) Dahal, A.; Dohnalek, Z. Formation of Metastable Water Chains on Anatase TiO2 (101). *J. Phys. Chem. C* **2017**, *121*, 20413–20418.

(65) Kokubo, T. Apatite formation on surfaces of ceramics, metals and polymers in body environment. *Acta Mater.* **1998**, *46*, 2519–2527.

(66) Takadama, H.; Kim, H. M.; Kokubo, T.; Nakamura, T. An X-ray photoelectron spectroscopy study of the process of apatite formation on bioactive titanium metal. *J. Biomed. Mater. Res.* **2001**, *55*, 185–193.

(67) Mancardi, G.; Terranova, U.; de Leeuw, N. H. Calcium Phosphate Prenucleation Complexes in Water by Means of ab Initio Molecular Dynamics Simulations. *Cryst. Growth Des.* **2016**, *16*, 3353–3358.

Graphical TOC Entry